ARTICLE   OPEN

Symmetry-enforced nodal chain phonons

Jiaojiao Zhu[1], Weikang Wu [1,2 ✉], Jianzhou Zhao [1,3 ✉], Hao Chen[4], Lifa Zhang[4] and Shengyuan A. Yang [1]

Topological phonons in crystalline materials have been attracting great interest. Most cases studied so far are direct generalizations of the topological states from electronic systems. Here, we reveal a class of topological phonons - the symmetry-enforced nodal-chain phonons, which manifest the characteristic of phononic systems. We show that in five space groups with D_{2d} little co-group at a non-time-reversal-invariant-momentum point, the phononic nodal chain is guaranteed to exist owing to the vector basis symmetry of phonons, which is a character distinct from electronic and other systems. In other words, this symmetry enforcement feature of the proposed nodal chain is limited to phononic systems. Interestingly, the chains in these five space groups exhibit two different patterns: for tetragonal systems, they are one-dimensional along the fourfold axis; for cubic systems, they form a three-dimensional network structure. Based on first-principles calculations, we identify K_2O as a realistic material hosting the proposed nodal-chain phonons. We show that the effect of LO-TO splitting helps to expose the nodal-chain phonons in a large frequency window. In addition, the nodal chains may lead to drumhead surface phonon modes on multiple surfaces of a sample.

INTRODUCTION

Topological quasiparticles, emerged around band degeneracy points in condensed matters, have been attracting tremendous research interest in the past decade. The field was initiated with a focus on electronic systems. Pioneering examples include electrons around Weyl[1–4] and Dirac[4–8] points in the band structures, which resemble Weyl and Dirac fermions and thereby can simulate fascinating effects from high energy physics[9–11]. Moreover, condensed matter systems respect the space group (SG) symmetry, which is a much smaller subgroup of the Poincaré symmetry. The reduced constraints permit a rich variety of emergent quasiparticles beyond the Weyl/Dirac paradigm[12–15]. For instance, band degeneracies may form higher-dimensional manifolds in the momentum space, leading to nodal-line[7,16–25] and even nodal-surface[26–29] electrons, with topological boundary modes and effects.

It was later realized that this research can be naturally extended to bosonic and even classical systems. Particularly, there is a surge of interest recently in exploring quasiparticles in phonons[30–36], which describe the atomic lattice vibrations in solids. This is also motivated by the advance in experimental techniques which can now probe the full THz phonon spectrum with meV-resolution[37–39]. A number of materials with Weyl, Dirac, and nodal-line phonons have been predicted[40–47], and some have been successfully verified in experiment[43,48]. As direct extensions of corresponding concepts from electronic systems, except for the particles statistics, most of these phonons share essentially the same features as their electronic counterparts.

In this work, we try to find topological phonons with a character limited to phononic systems. Specifically, we present such an example - the symmetry-enforced nodal-chain phonons.

A nodal chain is composed of multiple nodal rings touching at isolated points and is extended in momentum space (e.g., see Fig. 1). The concept was initially studied also in electronic systems,

where the electronic nodal chains usually require complicated non-symmorphic crystal symmetries to be robust against spin-orbit coupling (SOC)[49,50]. Nodal chains with symmorphic symmetries were also discussed[51–54], but they are typically destroyed by SOC, and more importantly, they are not symmetry enforced, meaning that their presence in the spectrum depends on the system details and is not guaranteed.

In this work, we find a class of nodal-chain phonons that are enforced by symmorphic symmetries. We show that in five SGs, such phonons are enforced by the D_{2d} little co-group and its vector representation at a non-time-reversal-invariant-momentum (non-TRIM) point O. The key point is: Unlike electrons and other systems, where the basis at lattice sites can take different symmetries (e.g., *s*, *p*, *d*, etc.), for phonons, the lattice displacement at each site is a vector. For the five SGs, modes with the vector representation at O are guaranteed to exist due to the real-space vector basis symmetry. Therefore, the nodal chain is guaranteed to exist in these space groups. In addition, the vulnerability under SOC is not an issue here, since phonons are intrinsically spinless. In this sense, the proposed symmetry-enforced nodal chain indeed manifests characters for phononic systems. Interestingly, depending on the SG, there are two different nodal-chain patterns, as shown in Fig. 1. Guided by the symmetry condition, we propose that K_2O, an existing material, is a candidate with almost ideal nodal chain phonons. We show that the LO-TO splitting[55] helps to expose the phononic nodal chain in K_2O as the only band degeneracy in a large frequency window, facilitating the experimental detection. In addition, due to the spacetime inversion symmetry $\mathcal{PT}$, each ring in the chain enjoys additional protection by the π Berry phase[56], which also leads to the protected drumhead surface phonon modes[8,17] on multiple surfaces of a sample.

[1]Research Laboratory for Quantum Materials, Singapore University of Technology and Design, Singapore 487372, Singapore. [2]Division of Physics and Applied Physics, School of Physical and Mathematical Sciences, Nanyang Technological University, Singapore 637371, Singapore. [3]Co-Innovation Center for New Energetic Materials, Southwest University of Science and Technology, Mianyang 621010, China. [4]NNU-SULI Thermal Energy Research Center (NSTER) & Center for Quantum Transport and Thermal Energy Science (CQTES), School of Physics and Technology, Nanjing Normal University, Nanjing 210023, China. ✉email: weikang.wu@ntu.edu.sg; jzzhao@swust.edu.cn
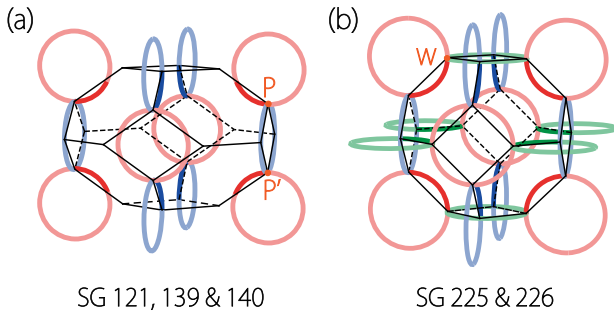
Fig. 1 Symmetry-enforced nodal chains for the five candidates SGs. a SG 121, 139, and 140 host nodal chains running along the fourfold S_{4z} axis. **b** In SG 225 and 226, there are chains running along all three directions, forming a network structure. Here, the rings with different orientations are marked with different colors.
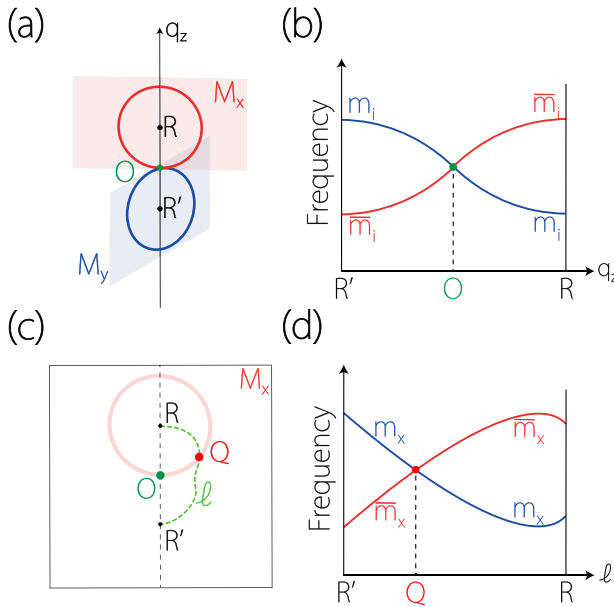

Fig. 2 Schematic diagram for a nodal chain. a Schematic diagram for a nodal chain formed by two rings located in two mutually orthogonal mirror planes M_x and M_y. O is a non-TRIM point with D_{2d} little co-group. **b** Spectrum along the q_z axis for a pair of phonon branches that correspond to the E representation of D_{2d} at O. m_i ($i = x, y$) are the mirror eigenvalues. **c** An arbitrary path ℓ in the M_x plane, which connects a point R on the q_z axis to its S_{4z} image R'. The spectrum along ℓ is shown in (**d**), where the two branches must still cross at some point Q, as they have opposite m_x eigenvalues. The crossing point traces out a ring in the M_x plane, as shown in (**c**).

RESULTS

Symmetry condition

First, we propose a formation mechanism for the phononic nodal chain. We show that the D_{2d} group with its vector representation at a non-TRIM point of the Brillouin zone (BZ) enforces the existence of a chain. The D_{2d} group contains two mutually orthogonal mirrors, which we may denote as M_x and M_y, and a fourfold roto-reflection S_{4z}, which connects the two mirrors. Assume that D_{2d} is the little co-group (or its subgroup) at a non-TRIM point O in the BZ, and the q_z axis through O corresponds to the S_{4z} axis, as shown in Fig. 2a.

Consider the modes at O which correspond to the two-dimensional vector irreducible representation E of D_{2d}. These modes transform as vectors lying in the plane normal to the S_{4z} axis. They form twofold degenerate pairs at O (each pair corresponding to the E representation). Let us consider one such

degenerate pair. Since $[M_x, M_y] = 0$, the two states can be chosen as simultaneous eigenstates of the two mirrors, and they must have opposite M_x as well as M_y eigenvalues. If we denote one state as $|m_x, m_y\rangle$ with $m_{x/y} \in \{+1, -1\}$ the mirror eigenvalues, then the other state must be $|\overline{m}_x, \overline{m}_y\rangle$, where $\overline{m}_i \equiv -m_i$. In the subspace of this pair, the symmetry operations satisfy the following relations

$$\{\mathcal{M}_x, \mathcal{S}_{4z}\} = 0, \quad \{\mathcal{M}_y, \mathcal{S}_{4z}\} = 0. \tag{1}$$

Here, the script symbols denote the symmetry operators represented in the subspace.

When moving along the q_z axis away from O, the degenerate pair will generally split. However, the symmetries M_x and M_y are preserved on the q_z axis. Consider the spectrum of the two branches on the q_z axis. First, it must be symmetric with respect to O, since the spectrum at point $(0, 0, q_z)$ is connected to that at $(0, 0, -q_z)$ by S_{4z}. Second, due to Eq. (1), the two states connected by S_{4z} at $(0, 0, \pm q_z)$ with the same energy must have opposite m_x and m_y values. This is schematically illustrated in Fig. 2b, showing that the two branches with opposite m_i ($i = x, y$) cross each other at O.

Now, consider an arbitrary path ℓ in the M_x plane, which connects a point R, say at $(0, 0, \pi/2)$, to its S_{4z} image R' at $(0, 0, -\pi/2)$ [see Fig. 2c]. Since ℓ is in the M_x plane, m_x for states on the path is still well defined. Meanwhile, because the m_x eigenvalues are flipped between R and R', the two phonon branches that we studied above must also cross each other at some point Q on the path ℓ, as illustrated in Fig. 2c, d. Since ℓ is arbitrary, the crossing point must trace out a nodal ring passing through O and lying in the M_x plane. The same argument applies to the M_y plane and results in another nodal ring. The two rings are perpendicular to each other, touch at point O [and also at $(0, 0, \pm\pi)$ which is another D_{2d}-invariant point], and are connected by S_{4z}. Therefore, they compose a nodal chain in the momentum space running along the S_{4z} axis, as illustrated in Fig. 2a.

We have a few remarks. First, we required point O to be a non-TRIM point. The reason is that if it is a TRIM point, then the time-reversal symmetry $\mathcal{T}$ and S_{4z} would require the two branches that are degenerate at O remain degenerate on the q_z axis. In this case, we have only a single phononic nodal line, rather than a chain.

Second, the touching of two perpendicular rings at the O point can also be inferred from the $k \cdot p$ effective model expanded at O. Constrained by the D_{2d} group and on the E basis, we obtain the following effective model expanded to q-quadratic order

$$\mathcal{H}_{\text{eff}}(\mathbf{q}) = \epsilon(\mathbf{q})\sigma_0 + c_1 q_x q_y \sigma_x + [c_2 q_z + c_3(q_x^2 - q_y^2)]\sigma_z, \tag{2}$$

where $\epsilon(\mathbf{q}) = \varepsilon_1(q_x^2 + q_y^2) + \varepsilon_2 q_z^2$, ε_i and c_i are real model parameters, and σ's are Pauli matrices. The model shows a linear band splitting along q_z and quadratic splitting in the q_x-q_y plane. The degeneracy manifold indeed conforms with that of two orthogonal nodal rings (see details in the Supplementary Information).

Third, the analysis above applies only to spinless particles. For spinful ones like electrons, the SOC will generally destroy the nodal chain[51].

Candidate space groups

Based on the proposed symmetry conditions above, we search for the candidate SGs through the 230 SGs. For each SG, we examine the little co-group for each non-TRIM high-symmetry point and check whether it contains D_{2d} as a subgroup. This screening results in 10 SGs, including SG 121, 122, 139, 140, 141, 142, 225, 226, 227, and 228.

After obtaining these SGs, we further check whether our proposed symmetry conditions are indeed fulfilled in these SGs. This is necessary because of two reasons. First, point O is not at the BZ center. The fractional translation in the certain non-symmorphic operations of the SG may alter the symmetry algebra

Table 1. SGs hosting the proposed symmetry-enforced nodal-chain phonons.

SG No.	Crystal system	Touching point
121	Tetragonal	$P(\frac{1}{4}, \frac{1}{4}, \frac{1}{4})$ $P'(-\frac{1}{4}, -\frac{1}{4}, \frac{3}{4})$
139	Tetragonal	$P(\frac{1}{4}, \frac{1}{4}, \frac{1}{4})$
140	Tetragonal	$P(\frac{1}{4}, \frac{1}{4}, \frac{1}{4})$
225	Cubic	$W(\frac{1}{2}, \frac{1}{4}, \frac{3}{4})$
226	Cubic	$W(\frac{1}{2}, \frac{1}{4}, \frac{3}{4})$

Here, the coordinates of the ring touching points (O point in Fig. 2a) are also provided. P and P' points are connected by symmetry in SG 139 and 140, but not in SG 121.

at such a point. Second, depending on the SG, there may be some additional symmetry, particularly some magnetic symmetry (of the form $U\mathcal{T}$ with U a spatial operation), at point O, which may affect the formation of the nodal chain. This process removes five of the ten SGs, for which the nodal chain would reduce to a straight nodal line along the S_{4z} axis due to additional non-symmorphic operations. The remaining five candidates SGs are listed in Table 1.

Among the five candidates SGs in Table 1, by using the MKVEC tool[57–61], we find that for SG 121, the magnetic little co-group at O is $-42\,m$, which is just D_{2d}. Meanwhile, for the other four SGs, the magnetic little co-group at O is $4'/m'm'm$, which is a supergroup of D_{2d} and contains the extra magnetic symmetry of $\mathcal{PT}$. Nevertheless, we verify that the extra $\mathcal{PT}$ symmetry does not affect the existence of the nodal chain in these SGs. The information of crystal system and the corresponding point O are also given in Table 1.

Next, we check that for these five SGs, the required vector representation at O must exist due to the real-space vector basis symmetry. Specifically, for each SG candidate, by using the BANDREP tool[62–64], we examine the representations at O induced by the (real-space) vector basis at all possible Wyckoff positions in a unit cell (see the Supplementary Information for details)[62]. Through this process, we confirm that the required vector representation and hence the nodal chain are guaranteed to appear in these five SGs. Clearly, from the analysis, the symmetry enforcement here originated from the vector basis symmetry of phononic systems. This symmetry enforcement mechanism is the most important characteristics of our proposed topological phonons.

Interestingly, the five SGs can give two different patterns of the nodal chains, as illustrated in Fig. 1. One observes that the chains in SG 121, 139, and 140 form a one-dimensional structure running along the S_{4z} axis. In comparison, there are three families of orthogonal chains for SG 225 and 226, forming a three-dimensional chain network.

In addition, we note that except for SG 121, the groups in Table 1 possess the inversion symmetry $\mathcal{P}$. Then for these SGs, the combined $\mathcal{PT}$ symmetry enforces a π-quantized Berry phase for arbitrarily closed loops in momentum space, constituting a one-dimensional $\mathbb{Z}_2$ topological charge for $\mathcal{PT}$-invariant systems. For SGs with mirror or certain rotation symmetries, the Berry phase can also be quantized on some loop, if the symmetry operation reverses the momentum on the loop. This offers the nodal rings additional protection, namely, each ring is protected by the π Berry phase defined on a small loop encircling the ring. As a result, even when the symmetry is reduced by certain perturbations on the system, each ring should persist as long as $\mathcal{PT}$ is still preserved.

Nodal-chain phonons in K$_2$O

Guided by the symmetry condition, we identify an existing material K$_2$O as a candidate with almost ideal nodal-chain phonons. The K$_2$O crystal was synthesized long ago in the

1930s[65]. As shown in Fig. 3a, it has the antifluorite crystal structure with the SG 225 ($Fm\overline{3}m$), which is one of the candidates in Table 1. We investigate its properties by using the first-principles calculations based on the density functional theory (DFT). The calculation details are presented in the Methods. The optimized conventional lattice constant is $a = 6.49$ Å, which agrees well with the experimental value of 6.44 Å[65]. The two types of atoms K and O occupy the 8c and 4a Wyckoff positions, respectively.

The calculated phonon spectrum of K$_2$O is plotted in Fig. 3c. According to Table 1 and Fig. 1b, for SG 225, the ring touching point O corresponds to the W point of the BZ, and there are three mutually orthogonal rings, forming a network of chains in the extended BZ. In Fig. 3c, a chain at around 7 THz formed by two optical branches can be clearly observed (indicated by the red arrows). A careful scan of the BZ confirms that the crossing between the top two branches forms the chain pattern consistent with Fig. 1b.

Notably, in Fig. 3c, the phonon band structure around the chain is not very "clean", because the top phonon branch bends down near the BZ center. Fortunately, this is remedied by including the non-analytic correction from long-range Coulomb interactions, which is typically pronounced for ionic crystals such as K$_2$O. This correction leads to the well-known energy splitting between longitudinal optical and transverse optical phonon branches near the BZ center, i.e., the LO-TO splitting. In Fig. 3d, one observes that the correction results in a large LO-TO splitting and pushes up the top branch. Meanwhile, the dispersion around the chain is more or less unaffected. Consequently, the phononic nodal chain is now well exposed in a large frequency window with a width ~1 THz. The energy of the chain can be readily inferred from the dip in the phonon density of states.

The phononic nodal chain here is guaranteed to exist in the spectrum, associated with the vector representation induced by the real-space vector basis. It should be noted that there are also other induced representations presenting at the same time, and the corresponding phonon branches do not form nodal chains. This is the case for the bands around 5 THz in Fig. 3.

The clean band structure, the relatively large frequency window, and the small energy variation on the chain make K$_2$O an almost ideal candidate for experimental studies of our proposed symmetry-enforced nodal-chain phonons.

Topological surface phonon modes

We have mentioned that owing to the $\mathcal{PT}$ symmetry, each ring of the chain features a quantized π Berry phase. It follows that the Zak phase, defined as the Berry phase along a straight line traversing the BZ, must change by π when the line crosses a ring. The π Zak phase is verified by our first-principles calculations, as indicated in Fig. 4a. It leads to the protected drumhead-like surface modes, which span the region in the surface BZ bounded by the projection of the ring.

In Fig. 4b, we plot the calculated surface phonon spectrum for the (001) surface of K$_2$O. One indeed finds the drumhead surface phonon modes, as indicated by the arrows. Drumhead surface modes also exist for conventional nodal-ring states, but they typically exist only on particular surfaces. For example, when the ring is parallel to the (001) surface, it is not going to produce drumhead surface modes on (100) and (010) surfaces. In comparison, since a nodal chain here is composed of orthogonal nodal rings, it must have drumhead surface modes simultaneously on multiple surfaces.

DISCUSSION

We have revealed a topological phonon state that manifests the features of phononic systems, namely, it is enforced to exist by the vector basis symmetry of phonons. With this understanding, our
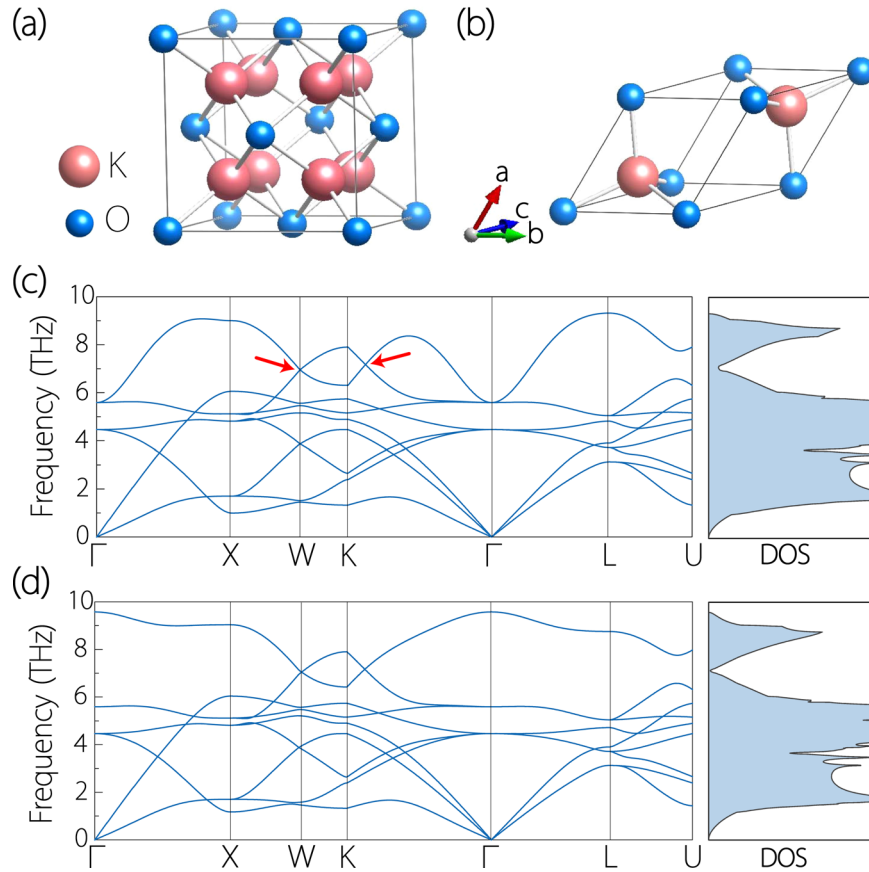
Fig. 3 Calculated phonon spectrum and phonon density of states for K$_2$O. a Conventional unit cell and (**b**) primitive cell of K$_2$O. **c** Calculated phonon spectrum and phonon density of states for K$_2$O. The arrows indicate points on the nodal chain. **d** Calculated phonon spectrum and phonon density of states with non-analytic correction (LO-TO splitting) included.
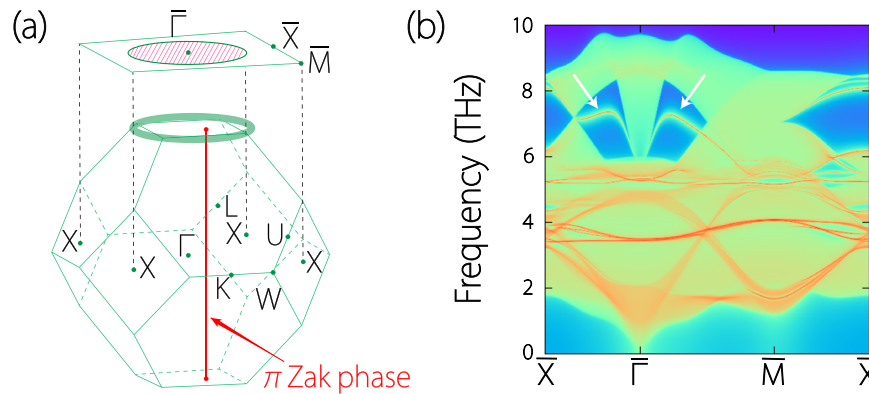

Fig. 4 Calculated surface phonon spectrum for the (001) surface of K$_2$O. a K$_2$O's BZ and the corresponding (001) surface BZ. A straight path passing through the nodal ring has a π Zak phase. This leads to protected drumhead surface modes. Here, we only show the ring in the horizontal plane. The analysis also applies to the other rings of the chain. **b** Calculated surface phonon spectrum for the (001) surface of K$_2$O (without non-analytic correction). The arrows indicate the drumhead surface phonon modes.

work will open the direction to explore more types of topological phonons that are enforced by the basis of symmetry.

As mentioned in the introduction part, there are also other types of nodal chains in both spinless and spinful systems. For example, ref. 53 reported a spinless nodal chain in the electronic band structures of some honeycomb layered structures. Different from our case, the ring contact point (*O* point) there is not fixed on a high-symmetry point but can move on a high-symmetry path; and more importantly, the chain there is not symmetry enforced but is of accidental type.

It should be noted that although our proposed phononic nodal chain is guaranteed to exist in certain SGs, its energy and dispersion still depend on the details of the system. Hence, identifying experimentally favorable material candidates still requires extensive effort and a degree of luck. Nevertheless, the symmetry conditions revealed here to provide useful guidance for the material search. Besides K$_2$O, we also identified a few other example materials, including Ge$_2$Zn$_4$Se$_8$ (SG 121), Te$_2$O$_4$Tb$_4$ (SG 139), and Ag$_4$Tl$_4$I$_8$ (SG 140), with the help of the phonon database [47].

In an experiment, the bulk phonon dispersion can be imaged by inelastic x-ray scattering (IXS)[37–39] or neutron scattering[66]. The surface phonon modes can be probed by the high-resolution electron energy loss spectroscopy[67], helium scattering[68], or THz spectroscopy[69,70]. Particularly, recent experiments with inelastic x-ray scattering have successfully mapped out topological phonons with meV-resolution, which is sufficient for detecting the nodal-chain phonons in K_2O.

Currently, the study of topological nodal phonons is still at an early stage, mostly driven by academic interest. These phonons may have impacts on observable physical properties or effects. For example, as argued by Singh et al.[41], phonon band crossings tend to introduce phonon-phonon scattering centers, which suppresses the lattice thermal conductivity and may enhance the thermo-electric performance. As for the drumhead surface phonon modes, Zhang et al.[43] suggested that they may induce surface electronic structure anomalies through electron-phonon coupling. This may promote the possibility of surface superconductivity. In addition, most catalytic processes also occur on the surfaces. The topological surface phonon modes may in some cases promote the catalysis if the phonon frequency is in resonance with certain mid steps in the reaction. Certainly, these are still preliminary speculations. Possible applications of these topological phonons will require more future research works.

Note added. During the review of our work, a work by Tang and Wan appeared[71], which did a systematic study of all band nodal structures in the 1651 magnetic space groups and 528 magnetic layer groups for both spinless and spinful systems. In the five-candidate space groups, their results are consistent with our analysis here.

METHODS

Details of first-principles calculations

Density functional theory (DFT) calculations were conducted by using the Vienna ab initio simulation package (VASP)[72,73]. The projector augmented wave (PAW) pseudopotentials were adopted in the calculation[74,75]. Generalized gradient approximation (GGA) in the form of Perdew–Burke–Ernzerhof (PBE)[76] realization was adopted for the exchange-correlation potential. The valence electrons treated in the calculations include K ($3s^23p^64s^1$) and O ($2s^22p^4$). The kinetic energy cutoff was fixed to 520 eV. Γ-centered $10 \times 10 \times 10$ k point mesh was adopted for the self-consistent calculations. The energy and force convergence criteria were set to be 10^{-7} eV and 0.001 eV Å^{-1}, respectively. We used density functional perturbation theory (DFPT)[77] in combination with the Phonopy package[78] to obtain the force constants and phonon spectra. A supercell of $3 \times 3 \times 3$ is adopted for the calculation of force constants. Nonanalytical correction (NAC) was considered in treating the long-range interaction of the macroscopic electric field induced by the polarization of the collective ionic motions near the Γ point, following the approach of ref.[79]. For computing the surface phonon spectrum, we first calculated the second rank tensor of force constant in Cartesian coordinates from DFPT, from which we can get the tight-binding parameters for the bulk and surface atoms[78]. Then we obtain the surface Green's function iteratively by using the WannierTools package[80–82].

DATA AVAILABILITY

The data sets that support the findings in this study are available from the corresponding author upon request.

CODE AVAILABILITY

The codes that support the findings in this study are available from the corresponding author upon request.

REFERENCES

1. Murakami, S. Phase transition between the quantum spin Hall and insulator phases in 3D: emergence of a topological gapless phase. *New J. Phys.* **9**, 356 (2007).
2. Wan, X., Turner, A. M., Vishwanath, A. & Savrasov, S. Y. Topological semimetal and Fermi-arc surface states in the electronic structure of pyrochlore iridates. *Phys. Rev. B* **83**, 205101 (2011).
3. Dai, X. Weyl fermions go into orbit. *Nat. Phys.* **12**, 727–728 (2016).
4. Armitage, N. P., Mele, E. J. & Vishwanath, A. Weyl and Dirac semimetals in three-dimensional solids. *Rev. Mod. Phys.* **90**, 015001 (2018).
5. Young, S. M. et al. Dirac semimetal in three dimensions. *Phys. Rev. Lett.* **108**, 140405 (2012).
6. Wang, Z. et al. Dirac semimetal and topological phase transitions in A_3Bi (A = Na, K, Rb). *Phys. Rev. B* **85**, 195320 (2012).
7. Wang, Z., Weng, H., Wu, Q., Dai, X. & Fang, Z. Three-dimensional Dirac semimetal and quantum transport in Cd_3As_2. *Phys. Rev. B* **88**, 125427 (2013).
8. Yang, S. A., Pan, H. & Zhang, F. Dirac and Weyl superconductors in three dimensions. *Phys. Rev. Lett.* **113**, 046401 (2014).
9. Nielsen, H. B. & Ninomiya, M. The Adler-Bell-Jackiw anomaly and Weyl fermions in a crystal. *Phys. Lett. B* **130**, 389–396 (1983).
10. Volovik, G. E. *The Universe in a Helium Droplet* (Oxford Univ. Press, 2009).
11. Guan, S. et al. Artificial gravity field, astrophysical analogues, and topological phase transitions in strained topological semimetals. *npj Quant. Mater.* **2**, 23 (2017).
12. Wieder, B. J., Kim, Y., Rappe, A. M. & Kane, C. L. Double Dirac semimetals in three dimensions. *Phys. Rev. Lett.* **116**, 186402 (2016).
13. Bradlyn, B. et al. Beyond Dirac and Weyl fermions: unconventional quasiparticles in conventional crystals. *Science* **353**, aaf5037 (2016).
14. Lv, B. Q., Qian, T. & Ding, H. Experimental perspective on three-dimensional topological semimetals. *Rev. Mod. Phys.* **93**, 025002 (2021).
15. Yu, Z.-M. et al. Encyclopedia of emergent particles in three-dimensional crystals. *Sci. Bull.* **67**, 375–380 (2022).
16. Burkov, A. A., Hook, M. D. & Balents, L. Topological nodal semimetals. *Phys. Rev. B* **84**, 235126 (2011).
17. Weng, H. et al. Topological node-line semimetal in three-dimensional graphene networks. *Phys. Rev. B* **92**, 045108 (2015).
18. Chen, Y. et al. Nanostructured carbon allotropes with Weyl-like loops and points. *Nano Lett.* **15**, 6974–6978 (2015).
19. Mullen, K., Uchoa, B. & Glatzhofer, D. T. Line of Dirac nodes in hyperhoneycomb lattices. *Phys. Rev. Lett.* **115**, 026403 (2015).
20. Fang, C., Chen, Y., Kee, H.-Y. & Fu, L. Topological nodal line semimetals with and without spin-orbital coupling. *Phys. Rev. B* **92**, 081201(R) (2015).
21. Yu, R., Weng, H., Fang, Z., Dai, X. & Hu, X. Topological node-line semimetal and Dirac semimetal state in antiperovskite Cu_3PdN. *Phys. Rev. Lett.* **115**, 036807 (2015).
22. Kim, Y., Wieder, B. J., Kane, C. L. & Rappe, A. M. Dirac line nodes in inversion-symmetric Crystals. *Phys. Rev. Lett.* **115**, 036806 (2015).
23. Zhao, J., Yu, R., Weng, H. & Fang, Z. Topological node-line semimetal in compressed black phosphorus. *Phys. Rev. B* **94**, 195104 (2016).
24. Fang, C., Weng, H., Dai, X. & Fang, Z. Topological nodal line semimetals. *Chin. Phys. B* **25**, 117106 (2016).
25. Yu, Z.-M., Wu, W., Sheng, X.-L., Zhao, Y. X. & Yang, S. A. Quadratic and cubic nodal lines stabilized by crystalline symmetry. *Phys. Rev. B* **99**, 121106(R) (2019).
26. Zhong, C. et al. Towards three-dimensional Weyl-surface semimetals in graphene networks. *Nanoscale* **8**, 7232–7239 (2016).
27. Liang, Q.-F., Zhou, J., Yu, R., Wang, Z. & Weng, H. Node-surface and node-line fermions from nonsymmorphic lattice symmetries. *Phys. Rev. B* **93**, 085427 (2016).
28. Bzdušek, T. & Sigrist, M. Robust doubly charged nodal lines and nodal surfaces in centrosymmetric systems. *Phys. Rev. B* **96**, 155105 (2017).
29. Wu, W. et al. Nodal surface semimetals: theory and material realization. *Phys. Rev. B* **97**, 115125 (2018).
30. Zhang, L., Ren, J., Wang, J.-S. & Li, B. Topological nature of the phonon Hall effect. *Phys. Rev. Lett.* **105**, 225901 (2010).
31. Zhang, L. & Niu, Q. Chiral phonons at high-symmetry points in monolayer hexagonal lattices. *Phys. Rev. Lett.* **115**, 115502 (2015).
32. Süsstrunk, R. & Huber, S. D. Classification of topological phonons in linear mechanical metamaterials. *Proc. Natl. Acad. Sci. USA* **113**, E4767–E4775 (2016).
33. Liu, Y., Lian, C.-S., Li, Y., Xu, Y. & Duan, W. Pseudospins and topological effects of phonons in a Kekulé lattice. *Phys. Rev. Lett.* **119**, 255901 (2017).
34. Ji, W.-C. & Shi, J.-R. Topological phonon modes in a two-dimensional Wigner crystal. *Chin. Phys. Lett.* **34**, 036301 (2017).
35. Liu, Y., Chen, X. & Xu, Y. Topological phononics: from fundamental models to real materials. *Adv. Funct. Mater.* **30**, 1904784 (2020).
36. Zhu, J. et al. Phononic real Chern insulator with protected corner modes in graphynes. *Phys. Rev. B* **105**, 085123 (2022).

37. Baron, A. Q. R. et al. Early commissioning of the SPring-8 beamline for high resolution inelastic X-ray scattering. *Nucl. Instrum. Methods Phys. Res. A: Accel. Spectrom. Detect. Assoc. Equip.* **467–468**, 627–630 (2001).

38. Mohr, M. et al. Phonon dispersion of graphite by inelastic x-ray scattering. *Phys. Rev. B* **76**, 035439 (2007).

39. Baron, A. Q. R. High-resolution inelastic X-ray scattering I: Context, spectrometers, samples, and superconductors, in *Synchrotron Light Sources and Free-Electron Lasers* (Springer International Publishing, 2015).

40. Zhang, T. et al. Double-Weyl phonons in transition-metal monosilicides. *Phys. Rev. Lett.* **120**, 016401 (2018).

41. Singh, S., Wu, Q., Yue, C., Romero, A. H. & Soluyanov, A. A. Topological phonons and thermoelectricity in triple-point metals. *Phys. Rev. Mater.* **2**, 114204 (2018).

42. Xia, B. W., Wang, R., Chen, Z. J., Zhao, Y. J. & Xu, H. Symmetry-protected ideal type-II Weyl phonons in CdTe. *Phys. Rev. Lett.* **123**, 065501 (2019).

43. Zhang, T. T. et al. Phononic helical nodal lines with $\mathcal{PT}$ protection in MoB_2. *Phys. Rev. Lett.* **123**, 245302 (2019).

44. Liu, Q.-B., Qian, Y., Fu, H.-H. & Wang, Z. Symmetry-enforced Weyl phonons. *npj Comput. Mater.* **6**, 95 (2020).

45. Huang, X., Deng, W., Li, F., Lu, J. & Liu, Z. Ideal type-II Weyl phase and topological transition in phononic crystals. *Phys. Rev. Lett.* **124**, 206802 (2020).

46. Wang, R. et al. Symmetry-protected topological triangular Weyl complex. *Phys. Rev. Lett.* **124**, 105303 (2020).

47. Li, J. et al. Computation and data driven discovery of topological phononic materials. *Nat. Commun.* **12**, 1204 (2021).

48. Miao, H. et al. Observation of double Weyl phonons in parity-breaking FeSi. *Phys. Rev. Lett.* **121**, 035302 (2018).

49. Bzdušek, T., Wu, Q., Rüegg, A., Sigrist, M. & Soluyanov, A. A. Nodal-chain metals. *Nature* **538**, 75–78 (2016).

50. Wang, S.-S., Liu, Y., Yu, Z.-M., Sheng, X.-L. & Yang, S. A. Hourglass Dirac chain metal in rhenium dioxide. *Nat. Commun.* **8**, 1844 (2017).

51. Yu, R., Wu, Q., Fang, Z. & Weng, H. From nodal chain semimetal to Weyl semimetal in HfC. *Phys. Rev. Lett.* **119**, 036401 (2017).

52. Chang, G. et al. Topological Hopf and chain link semimetal states and their application to Co_2MnGa. *Phys. Rev. Lett.* **119**, 156401 (2017).

53. Yan, Q. et al. Experimental discovery of nodal chains. *Nat. Phys.* **14**, 461–464 (2018).

54. Gong, C., Xie, Y., Chen, Y., Kim, H.-S. & Vanderbilt, D. Symmorphic intersecting nodal rings in semiconducting layers. *Phys. Rev. Lett.* **120**, 106403 (2018).

55. Zhong, W., King-Smith, R. D. & Vanderbilt, D. Giant LO-TO splittings in perovskite ferroelectrics. *Phys. Rev. Lett.* **72**, 3618–3621 (1994).

56. Zak, J. Berry's phase for energy bands in solids. *Phys. Rev. Lett.* **62**, 2747–2750 (1989).

57. Aroyo, M. I. et al. Bilbao crystallographic server: I. Databases and crystallographic computing programs. *Z. Kristallogr. Cryst. Mater.* **221**, 15–27 (2006).

58. Aroyo, M. I., Kirov, A., Capillas, C., Perez-Mato, J. M. & Wondratschek, H. Bilbao crystallographic server. II. Representations of crystallographic point groups and space groups. *Acta Crystallogr. A* **62**, 115–128 (2006).

59. Aroyo, M. I. et al. Crystallography online: Bilbao crystallographic server. *Bulg. Chem. Commun.* **43**, 183–197 (2011).

60. Xu, Y. et al. High-throughput calculations of magnetic topological materials. *Nature* **586**, 702–707 (2020).

61. Elcoro, L. et al. Magnetic topological quantum chemistry. *Nat. Commun.* **12**, 5965 (2021).

62. Bradlyn, B. et al. Topological quantum chemistry. *Nature* **547**, 298–305 (2017).

63. Vergniory, M. G. et al. Graph theory data for topological quantum chemistry. *Phys. Rev. E* **96**, 023310 (2017).

64. Elcoro, L. et al. Double crystallographic groups and their representations on the Bilbao crystallographic server. *J. Appl. Crystallogr.* **50**, 1457–1477 (2017).

65. Zintl, E., Harder, A. & Dauth, B. Gitterstruktur der oxyde, sulfide, selenide und telluride des lithiums, natriums und kaliums. *Z. Elektrochem.* **40**, 588–593 (1934).

66. Delaire, O. et al. Heavy-impurity resonance, hybridization, and phonon spectral functions in $Fe_{1-x}M_xSi(M = Ir, Os)$. *Phys. Rev. B* **91**, 094307 (2015).

67. Zhu, X. et al. High resolution electron energy loss spectroscopy with two-dimensional energy and momentum mapping. *Rev. Sci. Instrum.* **86**, 083902 (2015).

68. Harten, U. & Toennies, J. P. Surface phonons on GaAs(110) measured by inelastic helium atom scattering. *Europhys. Lett.* **4**, 833–838 (1987).

69. Wu, L. et al. High-resolution Faraday rotation and electron-phonon coupling in surface states of the bulk-insulating topological insulator $Cu_{0.02}Bi_2Se_3$. *Phys. Rev. Lett.* **115**, 217602 (2015).

70. Wu, L. et al. Quantized Faraday and Kerr rotation and axion electrodynamics of a 3D topological insulator. *Science* **354**, 1124–1127 (2016).

71. Tang, F. & Wan, X. Complete classification of band nodal structures. Preprint at https://arxiv.org/abs/2201.09836 (2022).

72. Kresse, G. & Furthmüller, J. Efficient iterative schemes for ab initio total-energy calculations using a plane-wave basis set. *Phys. Rev. B* **54**, 11169–11186 (1996).

73. Kresse, G. & Furthmüller, J. Efficiency of ab-initio total energy calculations for metals and semiconductors using a plane-wave basis set. *Comput. Mater. Sci.* **6**, 15–50 (1996).

74. Blöchl, P. E. Projector augmented-wave method. *Phys. Rev. B* **50**, 17953–17979 (1994).

75. Kresse, G. & Joubert, D. From ultrasoft pseudopotentials to the projector augmented-wave method. *Phys. Rev. B* **59**, 1758–1775 (1999).

76. Perdew, J. P., Burke, K. & Ernzerhof, M. Generalized gradient approximation made simple. *Phys. Rev. Lett.* **77**, 3865–3868 (1996).

77. Gonze, X. & Lee, C. Dynamical matrices, born effective charges, dielectric permittivity tensors, and interatomic force constants from density-functional perturbation theory. *Phys. Rev. B* **55**, 10355–10368 (1997).

78. Togo, A. & Tanaka, I. First principles phonon calculations in materials science. *Scr. Mater.* **108**, 1–5 (2015).

79. Gonze, X., Charlier, J.-C., Allan, D. C. & Teter, M. P. Interatomic force constants from first principles: the case of α-quartz. *Phys. Rev. B* **50**, 13035(R) (1994).

80. Sancho, M. P. L., Sancho, J. M. L. & Rubio, J. Quick iterative scheme for the calculation of transfer matrices: application to Mo (100). *J. Phys. F: Met. Phys.* **14**, 1205–1215 (1984).

81. Sancho, M. P. L., Sancho, J. M. L. & Rubio, J. Highly convergent schemes for the calculation of bulk and surface Green functions. *J. Phys. F: Met. Phys.* **15**, 851–858 (1985).

82. Wu, Q., Zhang, S., Song, H.-F., Troyer, M. & Soluyanov, A. A. WannierTools: an open-source software package for novel topological materials. *Comput. Phys. Commun.* **224**, 405–416 (2018).

ACKNOWLEDGEMENTS

AUTHOR CONTRIBUTIONS

J.J.Z., W.W., and J.Z.Z. performed the first-principles calculation and the data analysis. J.J.Z., W.W., H.C., and L.Z. contributed to the analytical modeling. S.A.Y., W.W., and J.Z.Z. supervised the work. J.J.Z., W.W., and S.A.Y. wrote the manuscript. All authors contributed to the discussion and reviewed the manuscript.

COMPETING INTERESTS

The authors declare no competing interests.

ADDITIONAL INFORMATION

Supplementary information The online version contains supplementary material available at https://doi.org/10.1038/s41535-022-00461-7.

Correspondence and requests for materials should be addressed to Weikang Wu or Jianzhou Zhao.

Reprints and permission information is available at http://www.nature.com/reprints

Publisher's note Springer Nature remains neutral with regard to jurisdictional claims in published maps and institutional affiliations.